COMPUTATIONAL PHANTOM FOR RED BONE MARROW DOSIMETRY FROM INCORPORATED BETA EMITTERS IN A NEWBORN BABY

Sharagin PA[1] ✉, Shishkina EA[1,2], Tolstykh EI[1]

[1] Urals Research Center for Radiation Medicine of the Federal Medical-Biological Agency, Chelyabinsk, Russia

[2] Chelyabinsk State University, Chelyabinsk, Russia

Active (red) bone marrow (AM) exposure due to ingested bone-seeking radionuclides can lead to grave medical consequences. For example, a radioactive contamination of the Techa River in the 1950s caused exposure to AM for riverside residents and led to chronic radioactive exposure syndrome in some of them, with higher risk of leukemia. The main sources of the marrow exposure were the bone-seeking beta emitters ^{89,90}Sr. Improving the dosimetry of AM internal exposure is an important step in clarifying the risks of chronic radiation exposure for riverside residents. To evaluate the energy absorbed by AM from incorporated ^{90}Sr it is customary to use computational phantoms where radiation transport can be emulated. A phantom is a representative digital representation of skeletal bone geometry and AM The goal of this work was to develop a computational phantom of a newborn skeleton for dosimetry of AM from incorporated ^{90}Sr. The researchers have used the Stochastic Parametric Skeletal Dosimetry method (SPSD), where hematopoietic sites were modeled as a set of phantoms of simple geometric shape describing individual skeletal bone areas. The AM content in the skeleton as well as the phantom parameters were evaluated on the basis of published measurements of real bones. As a result, a computational phantom of the main skeletal hematopoietic sites was generated for a newborn baby, including 34 phantoms of bone areas. The simulated phantom simulates the bone structure as well as the variability of skeletal parameters within the population and corresponds well to measurements of real bones.

Keywords: active bone marrow, trabecular bone, cortical bone, bone marrow dosimetry, computational phantoms, ^{90}Sr

Funding: The work was performed within the framework of the Federal Targeted Program "Nuclear and Radiation Safety" and was financially supported by the Federal Medical — Biological Agency of Russia. The methodological approaches were developed with financial support from the Federal Medical — Biological Agency of Russia and the Office of International Health Programs of the U.S. Department of Energy as part of the joint U.S.-Russian JCCRER 1.1 project.

Author contribution: all authors contributed equally to the development of research methodology, data acquisition, analysis, and interpretation, and to the writing and editing of the article.

✉ **Correspondence should be addressed:** Pavel Alekseevich Sharagin
Vorovskogo, 68-a, Chelyabinsk, 454141, Russia; sharagin@urcrm.ru

Received: 10.11.2022 **Accepted:** 19.12.2022 **Published online:** 27.12.2022

DOI: 10.47183/mes.2022.045

ВЫЧИСЛИТЕЛЬНЫЙ ФАНТОМ ДЛЯ ДОЗИМЕТРИИ КРАСНОГО КОСТНОГО МОЗГА НОВОРОЖДЕННОГО РЕБЕНКА ОТ ИНКОРПОРИРОВАННЫХ БЕТА-ИЗЛУЧАТЕЛЕЙ

П. А. Шарагин[1] ✉, Е. А. Шишкина[1,2], Е. И. Толстых[1]

[1] Уральский научно-практический центр радиационной медицины Федерального медико-биологического агентства России, Челябинск, Россия

[2] Челябинский государственный университет, Челябинск, Россия

Внутреннее облучение красного костного мозга (ККМ), обусловленное техногенными остеотропными радионуклидами, может приводить к серьезным медицинским последствиям. Так, радиоактивное загрязнение реки Течи в 1950-е годы стало причиной облучения ККМ у жителей прибрежных территорий, что привело к возникновению хронического лучевого синдрома у некоторых из них, а также повысило риск развития лейкозов в когорте этих жителей. Основными источниками внутреннего облучения ККМ были остеотропные бета-излучатели ^{89,90}Sr. Усовершенствование дозиметрии внутреннего облучения ККМ является важным этапом уточнения рисков хронического радиационного воздействия для жителей прибрежных территорий. Для оценки поглощенной энергии в ККМ от инкорпорированного ^{90}Sr используют вычислительные фантомы, в которых можно имитировать транспорт излучений. Фантом — это репрезентативное цифровое представление геометрии костей скелета и ККМ. Целью работы было разработать вычислительный фантом скелета новорожденного ребенка для дозиметрии ККМ от инкорпорированного ^{90}Sr. Для моделирования скелета использовали оригинальную методику SPSD (Stochastic parametric skeletal dosimetry): участки скелета с активным гемопоэзом моделировали как набор фантомов простой геометрической формы, описывающих отдельные участки костей скелета. Содержание ККМ в скелете, а также параметры фантомов оценивали на основе опубликованных результатов измерений реальных костей. В результате был сгенерирован вычислительный фантом основных участков скелета с активным гемопоэзом для новорожденного ребенка, включающий 34 фантома участков костей. Смоделированный фантом имитирует структуру костной ткани, а также вариабельность параметров скелета внутри популяции и хорошо соответствует измерениям реальных костей.

Ключевые слова: красный костный мозг, трабекулярная кость, кортикальная кость, дозиметрия костного мозга, вычислительные фантомы, ^{90}Sr

Финансирование: работа выполнена в рамках реализации федеральной целевой программы «Обеспечение ядерной и радиационной безопасности» и при финансовой поддержке Федерального медико-биологического агентства России. Методологические подходы были разработаны при финансовой поддержке Федерального медико-биологического агентства России и Управления международных программ здравоохранения Министерства энергетики США в рамках совместного американо-российского проекта JCCRER 1.1.

Вклад авторов: все авторы внесли равнозначный вклад в разработку методики исследования, получение, анализ и интерпретацию данных, в написание и редактирование статьи.

✉ **Для корреспонденции:** Павел Алексеевич Шарагин
ул. Воровского, д. 68-а, г. Челябинск, 454141, Россия; sharagin@urcrm.ru

Статья получена: 10.11.2022 **Статья принята к печати:** 19.12.2022 **Опубликована онлайн:** 27.12.2022

DOI: 10.47183/mes.2022.045

Active marrow (AM) exposure due to internal radiation from man-made bone-seeking radionuclides can lead to grave medical consequences. Such exposure can occur both as part of radionuclide therapy and due to radionuclides have been released into the environment as a result of nuclear weapons testing or radiation accidents. Radioactive contamination of the Techa River in the 1950s led to exposure AM of riverside village residents to doses of about 0.35 Gy, which caused chronic radiation syndrome [1–4] and an increased risk of leukemia. The main sources of AM internal exposure were the bone-seeking beta emitters ^{89,90}Sr [2]. This demonstrates that improvement of AM dosimetry from incorporated ^{90}Sr is an urgent task of radiobiology and radiation protection. ^{90}Sr dosimetry includes biokinetic modeling to estimate its distribution in body tissues and calculate the specific activity of ^{90}Sr in the source tissues, as well as dosimetric modeling of energy transfer from the source tissue (bone) to the target tissue (AM). The results of dosimetric modeling are dose factors (DF), which allow converting the specific activity of the incorporated radiation source into the absorbed dose rate in the target tissue. An important step in dosimetric modeling is the development of computational phantoms, i.e., a representative digital representation of source and target tissue geometries in which researchers can model the radiation transport. The bone is an object of modelling when constructing phantoms for AM dosimetry. The dosimetric bone model is a simplified representation of a real bone; it consists of a solid cortical bone layer that covers the phantom from the outside, whereas the spongiosa fills the model from the inside. Spongiosa is a set of trabecular bone, which modeled as a network of rod-like trabeculae and the AM located between them. Currently, there are several approaches for modeling the shape and structure of bone, based on the analysis of computed tomography (CT) images [5–9]. These methods require pathoanatomic material and do not allow taking into account the individual variability of the size of human bones. Instead, in the Urals Research Centre for Radiation Medicine" was developed an original parametric method for stochastic modeling of bone structures, known as SPSD modeling (stochastic parametric skeletal dosimetry) [10]. This method is based on the use of published averaged measurements of bone structures as phantom parameters, thus avoiding using of autopsy material, and assessing uncertainties associated with skeletal variability in different individuals.

The aim of this study is to develop a computational phantom of newborn skeleton for AM dosimetry from incorporated ^{90}Sr.

METHODS

The original SPSD technique was used for the skeleton modeling. In the frame of this approach, only skeletal areas with active hematopoiesis, i.e., those containing AM (hematopoietic sites), are modeled. The SPSD phantom of skeletal hematopoietic sites consist of a set of smaller phantoms — the Bone Phantom Segments (BPS) of a simple geometric shape, describing individual skeletal bone sites. Each phantom includes a description of the simulated media and a description of the source and target tissue geometries.

The modeled skeletal sites with active hemopoiesis (hemopoietic sites) were identified according to published data on AM distribution.

Each BPS consists of mineralized bone tissue and AM. To simulate the transport of energy in these two medias, we determined their chemical composition and density according to published data. These characteristics were used as parameters for all phantoms.

We evaluated parameters characterizing irradiation geometry for each BPS: linear bone dimensions, cortical layer thickness (*Ct.Th*), trabecular thickness (*Tb.Th*), trabecular separation (*Tb.Sp*.), bone fraction in spongiosa volume (*BV/TV*). We evaluated the listed parameters based on published data. To assess the characteristics of bone geometry, articles in peer-reviewed publications, atlases, manuals, monographs and theses were considered. Also, we analyzed electronic resources containing collections of X-rays. The results of measurements of people/samples, which the authors identified as healthy and without diseases leading to bone deformation, were taken for analysis. Ethnically people/samples belonged to Caucasians and Mongolians due to the fact that these groups are characteristic of the population of the Ural region. We considered data from measurements of skeletal bones using various techniques: micrometers, anatomical boxes, ultrasound and radiological studies, CT (for linear dimensions and *Ct.Th*), histomorphometry and micro-CT — for microarchitecture parameters (*Tb.Th, Tb.Sp, BV/TV*). Averaged estimates of bone characteristics were taken as parameters of digital phantoms. If published data on individual measurements were available, we combined them and calculated arithmetic means and standard deviations (*SDs*). In the case of averaging the results of studies of groups of people, we would introduce a weighting coefficient (*Wn*), which took into account the number (*n*) of the studied subjects: $Wn = 1$, if $n \geq 25$; $Wn = n/25$ if $n < 25$. Methods for the selection and analysis of literature data are described in detail [11–14].

Based on the average values of the selected parameters for each bone segment, using the original Trabecula software [15] a computational phantom in voxel form — Bone Phantom Segment (BPS) was generated. BPS is a model of a simple geometric shape (rectangular parallelepiped, cylinder, prism, etc.), filled inside with spongiosa and on the outside covered with a cortical layer, as shown by the example of the phantom of the iliac bone of a newborn (Fig. 1).

Each phantom element (AM, trabecula, cortical layer) was imitated by a set of three-dimensional elements – voxels – from which simulated structures were composed. Each voxel imitate either mineralized bone or bone marrow (BM), depending on the location of the voxel center in the phantom. As source tissues, the dosimetric model considers trabecular bone (TB) and cortical bone (CB) separately, and bone marrow is considered as a target tissue, assuming that AM is uniformly distributed inside the BPS. The voxel size differed between phantoms, did not exceed 70% of the trabecula thickness [15, 16], and varied from 50 to 200 μm. Volumes of source and target tissues were automatically calculated in Trabecula software for each voxel phantom.

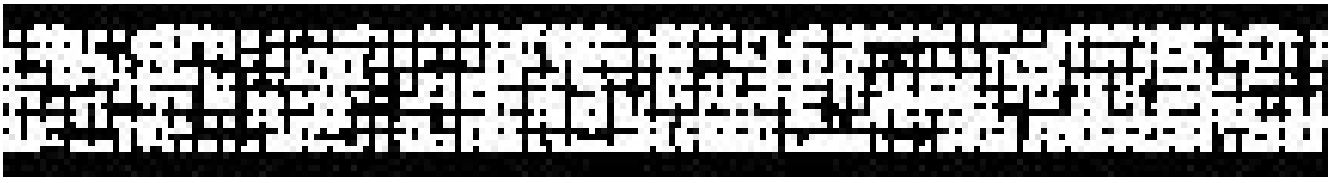

Fig. 1. Newborn's iliac phantom section (trabeculae's and cortical bone are shown in *black*, red bone marrow is shown in *white*)

Table 1. Mass fraction of AM (% of the total mass of AM in the skeleton) in the main hematopoietic sites of the skeleton of a newborn baby [17]

№	Hematopoietic site	AM mass fraction, %
1	Femur	6,7
2	Humeri	4,5
3	Sacrum	4,4
4	Tibia bones	7,1
5	Pelvic bones	11,4
6	Skull	28,2
7	Clavicle	0,7
8	Scapula	2,3
9	Ribs	7,1
10	Radius and ulna	2,4
11	Hand and foot bones	10,8
12	Cervical vertebrae	1,7
13	Thoracic vertebrae	7,2
14	Lumbar vertebrae	5,5

To simulate population variability of size and microstructure characteristics, 12 Supplementary Phantom Segments (SPS) were created with parameters randomly selected within the range of their population variability (within the limits of minimum and maximum measured values) for each BPS.

RESULTS

The main hematopoietic sites of a newborn's skeleton and the mass fraction of AM in them were determined according to the data of MRI studies [17] and are presented in Table 1.

The phantom of skeletal hematopoietic sites of a newborn baby includes 14 hematopoietic sites. AM content of these varies from 1.7 to 28.2%.

Hematopoietic sites include bone regions that were not modeled in the SPSD approach. So, epiphyses of long bones were not modeled, since they are mostly composed of cartilage tissue [18–22]. We did not model the bones of the facial skull, since its share compared to the brain is about 13%, and a significant part of the body of the maxilla and mandibula is occupied by developing teeth [33–35]. Besides, vertebral processes were not modeled, since only small ossification centers are observed in newborns [23].

The chemical composition of the simulated medias was selected based on ICRP data for adults [19]. The chemical composition of bone tissue and the AM used for all BPS is presented in Table 2.

The density of mineralized bone tissue was estimated based on the results of measurements of the cortical bone density of newborns [24] and is 1.65 g/cm^3. The density of the red bone marrow was taken equal to the density of water (1 g/cm^3) [25].

We estimated the parameters of the spongiosa microarchitecture based on published data already described in detail [14]. The linear dimensions and thickness of the cortical layer as BPS parameters are presented in Table 3.

Thus, the phantom of skeletal hematopoietic sites of a newborn consist of 34 BPSs. Depending on the form of the simulated hematopoietic site, it may include 1 (ribs) to 5 (sacrum) BPSs. Most of the BPSs are cylinders and rectangular parallelepipeds. The sizes of phantoms vary widely: from 2 to 33 mm. As shown in Table 3, not all phantoms are covered with a cortical layer, which is associated with an incomplete process of ossification of the spine and skull bones. The highest *Ct.Th* value for a newborn is characteristic of the diaphysis of the femur (1.7 mm).

DISCUSSION

To test the adequacy of the SPSD approach, we performed a comparison of simulated phantoms and real bones. There are unique data on the mass of wet mineralized bones obtained during the study of 40 full-term newborns [68]. Masses corresponding to the sizes of phantoms were calculated as the sum of the volumes of simulated medias (BM, TB, CB) multiplied by their density.

Table 2. Chemical composition of simulated media adopted for all BPS

Chemical composition, rel. unit		
Chemical element	Bone	Active marrow
H	0,035	0,105
C	0,16	0,414
N	0,042	0,034
O	0,445	0,439
Na	0,003	0,001
Mg	0,002	0,002
P	0,095	0,002
S	0,003	0,002
Ca	0,215	–

Table 3. Linear dimensions and cortical thickness accepted for BPS of a newborn baby

Hematopoietic site	Segment	Shape[1]	Phantom parameters, mm (CV, % is in parentheses)[2]						References
			h	*a*	*b*	*c*	*d*	*Ct.Th.*	
Femur	Diaphysis[4]	c	30	7.2 (11)	7.2 (11)	–	–	1.7 (24)	26–32
	Proximal end	dc	19 (5)	26 (9)	12 (12)	7.2 (11)	7.2 (11)	0.5 (24)	
	Distal end	dc	19 (5)	26 (9)	12 (12)	7.2 (11)	7.2 (11)	0.4 (24)	
Humeri	Diaphysis tube[4]	c	30	6 (12)	6 (12)	–	–	1.3 (15)	26–31, 33
	Proximal end	dc	13 (10)	13 (12)	13 (12)	6 (12)	6 (11)	0.4 (15)	
	Distal end	dc	13 (10)	17 (13)	6 (12)	6 (12)	6 (11)	0.3 (19)	
Ribs	Ribs[4]	p	5.7 (38)	30	3.2 (12)	–	–	0.4 (37)	34, 35
Sacrum	Body of the 1st vertebra	p	6.3 (21)	15 (10)	7.5 (10)	–	–	–	36–39
	Body of the 2nd vertebra	p	6.3 (21)	12 (10)	6 (10)	–	–	–	
	Body of the 3rd vertebra	p	5.7 (19)	8.9 (10)	5.3 (9)	–	–	–	
	Body of the 4th vertebra	p	3.8 (21)	8.9 (10)	5.3 (9)	–	–	–	
	Body of the 5th vertebra	p	3.8 (21)	7.5 (10)	3.8 (11)	–	–	–	
Tibia bones	Fibula [4]	c	30	2.9 (7)	2.9 (7)	–	–	0.7 (14)	26, 30, 40
	Tibia diaphysis.[4]	c	30	6.9 (28)	6.9 (28)	–	–	1.4 (14)	26–29, 32, 41, 42
	Tibia proximal end	dc	19 (9)	21 (9)	13 (18)	6.9 (28)	6.9 (28)	0.3 (17)	
	Tibia distal end	dc	15 (9)	15 (23)	15 (23)	6.9 (28)	6.9 (28)	0.3 (17)	
Pelvic bones	Iliac bone part 1	p	4 (23)	24 (3)	24 (3)	–	–	1.2 (33) 0.5 (47)3	23, 43–47
	Iliac bone part 2	p	4 (23)	20 (3)	20 (3)	–	–	0.2 (25)	
	Pubic bone	c	16 (13)	7.5 (16)	7.5 (16)	–	–	0.4 (9)	
	Ischial bone	c	7.5 (16)	18 (11)	12 (8)	–	–	0.4 (9)	
Skull	Flat bones[4]	p	2 (25)	30	30	–	–	–	49–52
Clavicle	Body	c	33 (15)	4.3 (23)	5.9 (25)	–	–	0.8 (25)	53–58
	Sternum end	dc	5.9 (15)	12 (24)	10 (24)	5.9 (25)	4.3 (23)	0.3 (24)	
	Acromial end	dc	5.9 (15)	10 (24)	5.9 (49)	5.9 (25)	4.3 (23)	0.3 (24)	
Radius and ulna	Diaphysis[4]	c	30	3.9 (8)	3.9 (8)	–	–	0.9 (13)	26, 27, 29, 30, 41
	End	dc	12 (6)	5.8 (7)	5.8 (7)	3.9 (8)	3.9 (8)	0.3 (29)	
Hand and foot bones	Tubular bones	c	8.9 (43)	3.8 (42)	3.8 (42)	–	–	0.2 (25)	23, 53, 59,
	The talus and calcaneus	e	–	7.8 (14)	12 (11)	7.8 (14)	–	0.2 (25)	
Scapula	Glenoid	c	5.4 (4)	10 (21)	7.6 (18)	–	–	0.5 (29)	53, 60–63
	Acromion	p	7 (19)	16 (14)	13 (25)	–	–	0.4 (13)	
	Body[4]	p	2.7 (13)	30	30	–	–	0.4 (17)	
Cervical vertebrae	Vertebral body	c	4.1 (1)	6.9 (1)	6.5 (1)	–	–	–	64–66
Thoracic vertebrae	Vertebral body	c	5.1 (2)	7.6 (2)	11 (2)	–	–	–	66, 67
Lumbar vertebrae	Vertebral body	c	7.1 (1)	7.7 (1)	15 (1)	–	–	–	37, 66, 67

Note: [1] — the shape of the phantom was designated as follows: c — cylinder, dc — deformed cylinder, p-rectangular parallelepiped, e — ellipsoid; 2 — the dimensions of the BPS were designated as follows: *h* — height; *a* — major axis (c), major axis for a larger base (dc), or side *a* (p); *b* — minor axis (c), minor axis for a larger base (dc), or side b (*n*); *c* — major axis for a smaller base (dc); *d* — minor axis for a smaller base (dc); for an ellipsoid (e), *a*, *b*, *c* denote the axes of the ellipsoid; [3] — the thickness of the cortical layer was taken to be different for the inner (medial) and outer (gluteal) surfaces of this segment of the iliac bone (Fig. 1); [4] — the BPS imitated only a part of the simulated bone segment, if the dimensions of the bone segment significantly exceeded 30 mm, since in such cases, from the point of view of dosimetry, it does not have it makes no sense to model the entire bone section as a whole [11, 12].

A comparison of the measured bone masses and masses of SPSD phantoms (calculated as the sum of the masses of the segments describing the bone) is shown in Fig. 2.

As can be seen from the comparison, the masses corresponding to the sizes of SPSD phantoms in most cases fall within the range of standard deviation of the values obtained by the author of the compared work [68], that is, they correspond well to the masses of real bones.

A feature of the SPSD phantom is the generation by the BPS of a simple geometric shape, that is, a simplified representation of the real shape of the bone site. A simplified representation can result in biased estimates of simulation results. As mentioned earlier, BPS is modeled with mean population parameter values, and SPS parameters were randomly selected within their population variability range. As a result, the simulated bone segment is "inside" a set of SPSs

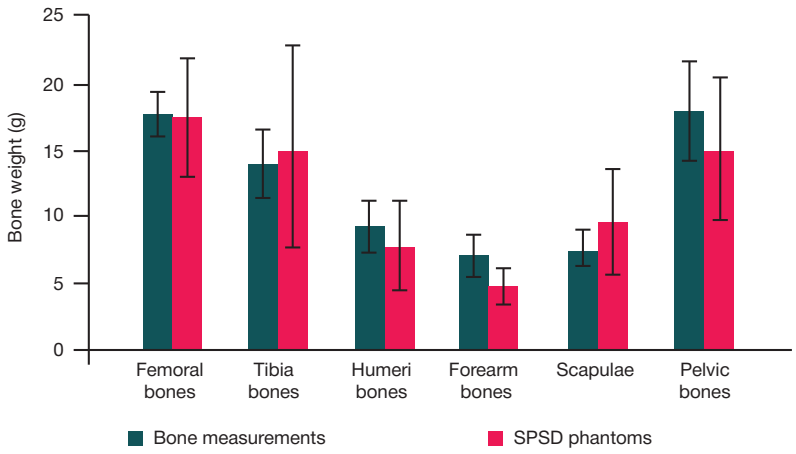

Fig. 2. Comparison of measured bone masses [68], and masses corresponding to the sizes of SPSD phantoms estimated as the sum of masses of all segments describing specific bones (left + right) of newborns, taking into account repeating and paired segments. Error bars showed the standard deviations."

geometric shapes. The variance of the DF set calculated for SPS reflects the effect of variability in bone size, shape, and microstructure.

CONCLUSIONS

As a result of the work, computational phantoms of the main skeletal sites with active hematopoiesis for a newborn were generated. The simulated phantom imitate the structure of bone tissue as well as the variability of skeletal parameters within a population. The phantom fits well with measurements of the newborn's real bones. The phantom is used to improve the the Techa River dosimetry system. In the future, SPSD phantoms will be created for other age groups: 1 year, 5 years, 10 years, 15 years, adults and for the human fetus at 24 weeks of pregnancy. SPSD phantoms can be used for dosimetry of other bone-seeking beta emitters including used in radionuclide therapy such as ^{89}Sr, ^{32}P, ^{186}Re, ^{188}Re, ^{117m}Sm.

References

1. Degteva MO, Shagina NB, Vorobiova MI, Shishkina EA, Tolstykh EI, Akleyev AV. Contemporary Understanding of Radioactive Contamination of the Techa River in 1949–1956. Radiats Biol Radioecol. 2016; 56 (5): 523–34. English, Russian. PMID: 30703313.
2. Krestinina LY, Epifanova S, Silkin S, Mikryukova L, Degteva M, Shagina N, Akleyev A. Chronic low-dose exposure in the Techa River Cohort: risk of mortality from circulatory diseases. Radiat Environ Biophys. 2013; 52 (1): 47–57. DOI: 10.1007/s00411-012-0438-5. Epub 2012 Nov 4.
3. Akleev AV. Xronicheskij luchevoj sindrom u zhitelej pribrezhnyx sel reki Techa. Chelyabinsk: Kniga, 2012; 464 s. Russian.
4. Preston DL, Sokolnikov ME, Krestinina LY, Stram DO. Estimates of Radiation Effects on Cancer Risks in the Mayak Worker, Techa River and Atomic Bomb Survivor Studies. Radiat Prot Dosimetry. 2017; 173 (1–3): 26–31. DOI: 10.1093/rpd/ncw316.
5. O'Reilly SE, DeWeese LS, Maynard MR, Rajon DA, Wayson MB, Marshall EL, et al. An 13 image-based skeletal dosimetry model for the ICRP reference adult female-internal electron 14 sources. Phys Med Biol. 2016; 61 (24): 8794–8824. Epub 2016 Nov 29.
6. Xu XG, Chao TC, Bozkurt A. VIP-Man: an image-based whole-body adult male model constructed from color photographs of the Visible Human Project for multi-particle Monte Carlo calculations. Health Phys. 2000; 78 (5): 476–86. DOI: 10.1097/00004032-200005000-00003. PMID: 10772019.
7. Shah AP, Bolch WE, Rajon DA, Patton PW, Jokisch DW. A paired-image radiation transport model for skeletal dosimetry. J Nucl Med. 2005; 46 (2): 344–53. PMID: 15695796.
8. Pafundi D. Image-based skeletal tissues and electron dosimetry models for the ICRP reference pediatric age series. A dissertation presented to the graduate schools of the University of Florida in partial fulfillment of the requirements for the degree of doctor of the philosophy. University of Florida, 2009.
9. Hough M, Johnson P, Rajon D, Jokisch D, Lee C, Bolch W. An image-based skeletal dosimetry model for the ICRP reference adult male–internal electron sources. Phys Med Biol. 2011; 56 (8): 2309–46. DOI: 10.1088/0031-9155/56/8/001. Epub 2011 Mar 22.
10. Degteva MO, Tolstykh EI, Shishkina EA, Sharagin PA, Zalyapin VI, Volchkova AYu, et al. Stochastic Parametric Skeletal Dosimetry model for humans: General description. PlosOne; 2021 (submitted).
11. Sharagin PA, Shishkina EA, Tolstykh EI, Volchkova AYu, Smith MA, Degteva MO. Segmentation of hematopoietic sites of human skeleton for calculations of dose to active marrow exposed to bone-seeking radionuclides. In: RAD Conference Proceedings, 2018; (3): 154–8. DOI: 10.21175/RadProc.2018.33.
12. Sharagin PA, Tolstykh EI, Shishkina EA, Degteva MO. Dozimetricheskoe modelirovanie kosti dlya osteotropnyx beta-izluchayushhix radionuklidov: razmernye parametry i segmentaciya. V sbornike: Materialy mezhdunarodnoj nauchnoj konferencii «Sovremennye problemy radiobiologii». Belarus', Gomel', 23–24 sentyabrya 2021. 2021; s. 200–204. Russian.
13. Tolstykh EI, Sharagin PA, Shishkina EA, Degteva MO. Formirovanie doz oblucheniya krasnogo kostnogo mozga cheloveka ot 89,90Sr, ocenka parametrov trabekulyarnoj kosti dlya dozimetricheskogo modelirovaniya. V sbornike: Materialy mezhdunarodnoj nauchnoj konferencii «Sovremennye problemy radiobiologii». Belarus', Gomel', 23–24 sentyabrya 2021. 2021; s. 176–179. Russian.
14. Tolstykh EI, Sharagin PA, Shishkina EA, Volchkova AYu. Degteva MO. Anatomo-morfologicheskij bazis dlya dozimetricheskogo modelirovaniya trabekulyarnoj kosti cheloveka s ispol'zovaniem stoxasticheskogo parametricheskogo podxoda. Klinicheskij vestnik GNC FMBC im.A. I. Burnazyana. 2022; 3: 25–40. Russian.
15. Shishkina EA, Timofeev YS, Volchkova AY, Sharagin PA, Zalyapin VI, Degteva MO, et al. Trabecula: A Random Generator of Computational Phantoms for Bone Marrow Dosimetry. Health Phys. 2020; 118 (1): 53–59. DOI: 10.1097/HP.0000000000001127.
16. Zalyapin VI, Timofeev YuS, Shishkina EA. A parametric stochastic model of bone geometry. Bulletin of Southern Urals State University, Issue «Mathematical Modelling. Programming & Computer Software» (SUSU MMCS). 2018; 11 (2): 44–57. DOI: 10.14529/mmp180204.

17. Cristy M. Active bone marrow distribution as a function of age in humans. Phys Med Biol. 1981; 26 (3): 389–400.
18. Vogler JB 3rd, Murphy WA. Bone marrow imaging. Radiology. 1988; 168 (3): 679–93.
19. Vande Berg BC, Malghem J, Lecouvet FE, Maldague B. Magnetic resonance imaging of the normal bone marrow. Skeletal Radiology. 1998; 27: 471–83.
20. Vande Berg BC, Malghem J, Lecouvet FE, Maldague B. Magnetic resonance imaging of normal bone marrow. Eur Radiol. 1998; 8 (8): 1327–34.
21. Taccone A, Oddone M, Dell'Acqua AD, Occhi M, Ciccone MA. MRI "road-map" of normal age-related bone marrow. II. Thorax, pelvis and extremities. Pediatr Radiol. 1995; 25 (8): 596–606; PubMed PMID: 8570312.
22. Taccone A, Oddone M, Occhi M, Dell'Acqua AD, Ciccone MA. MRI "road-map" of normal age-related bone marrow. I. Cranial bone and spine. Pediatr Radiol. 1995; 25 (8): 588–95; PubMed PMID: 8570311.
23. Cunningham C, Scheuer L, Black S. Developmental Juvenile Osteology. Elsevier Academic Press, 2016.
24. Robinson RA. Chemical analysis and electron microscopy of bone. In: Bone as a tissue, ed. by Rodahl K, Nicholson JT, Brown EM. New York: McGraw-Hill, 1960; p. 186–250.
25. Valentin J. Basic anatomical and physiological data for use in radiological protection: reference values. Annals of the ICRP. Annals of the ICRP. 32 (3–4): 1–277. 2002.
26. Medvedev MV. Ul'trazvukovaya fetometriya: spravochnye tablicy i nomogrammy. M.: Real'noe vremya, 2009; 19–24. Russian.
27. Florence JL. Linear and cortical bone dimensions as indicators of health status in subadults from the Milwaukee County Poor Farm Cemetery. M.A., University of Colorado at Denver, 2007.
28. Miles AEW. Growth Curves of Immature Bones from a Scottish Island Population of Sixteenth to mid-Nineteenth Century: Limb-bone Diaphyses and Some Bones of the Hand and Foot. International Journal of Osteoarcheology. 1994; 4: 121–36.
29. Maresh MM. Measurements from roentgenograms. In: Human Growth and Development (R.W. McCammon, Ed.). Springfield, IL: Charles C. Thomas, 1970; p. 157–200.
30. Jeanty P. Fetal limb biometry. Radiology. 1983; 147 (2): 601–2. DOI: 10.1148/radiology.147.2.6836145. PMID: 6836145.
31. Svadovsky VS. Age-related bone remodeling. Moscow, 1961.
32. Dhavale N, Halcrow SE, Buckley HR, Tayles N, Domett KM, Gray AR. Linear and appositional growth in infants and children from the prehistoric settlement of Ban Non Wat, Northeast Thailand: Evaluating biological responses to agricultural intensification in Southeast Asia, Journal of Archaeological Science: Reports. 2017; V11: 435–46.
33. Danforth ME, Wrobel GD, Armstrong CW, Swanson D. Juvenile age estimation using diaphyseal long bone lengths among ancient Maya populations. Latin American Antiquity. 2017; 20 (1): 3–13.
34. Beresheim AC, Pfeiffer S, Grynpas M. Ontogenetic changes to bone microstructure in an archaeologically derived sample of human ribs. J Anat. 2019. DOI: 10.1111/joa.13116.
35. Pfeiffer S. Cortical Bone Histology in Juveniles. Available from: https://www.researchgate.net/publication/303179375_Cortical_bone_histology_in_Juveniles
36. Hresko AM, Hinchcliff EM, Deckey DG, Hresko MT. Developmental sacral morphology: MR study from infancy to skeletal maturity. Eur Spine J. 2020. Available from: https://doi.org/10.1007/s00586-020-06350-6.
37. Mavrych V, Bolgova O, Ganguly P and Kashchenko S. Age-Related Changes of Lumbar Vertebral Body Morphometry. Austin J Anat. 2014; 1 (3): 7.
38. Dimeglio A, Bonnel F, Canavese F. The Growing Spine. In: Spinal Anatomy. Modern Concepts. Springer. 2020; 25–52.
39. Andronesky A. Anatomiya rebenka. Buxarest: Meridian, 1970. Russian.
40. Bernert Zs, Évinger S, Hajdu T. New data on the biological age estimation of children using bone measurements based on historical populations from the Carpathian Basin. Annales Historico-Naturales Musei Nationalis Hungarici. 2007; 99: 199–206.
41. Gindhart PS. Growth Standards for the Tibia and Radius in Children Aged One Month through Eighteen Years. Am J Phys Anthrop. 1973; 39: 41–48.
42. Suominen PK, Nurmi E, Lauerma K. Intraosseous access in neonates and infants: risk of severe complications - a case report. Acta Anaesthesiol Scand. 2015; 59 (10): 1389–93. DOI: 10.1111/aas.12602. Epub 2015 Aug 24. PubMed PMID: 26300243.
43. Blake KAS. An investigation of sex determination from the subadult pelvis: A morphometric analysis. Doctoral Dissertation, University of Pittsburgh. 2011.
44. Cunningham CA, Black SM. Iliac cortical thickness in the neonate — the gradient effect. J Anat. 2009; 215 (3): 364–70. DOI: 10.1111/j.1469-7580.2009.01112.x.
45. Cunningham CA, Black SM. Anticipating bipedalism: trabecular organization in the newborn ilium. J Anat. 2009; 214 (6): 817–29. DOI: 10.1111/j.1469-7580.2009.01073.x.
46. Corron L, Marchal F, Condemi S, Chaumoître K, Adalian P. A New Approach of Juvenile Age Estimation using Measurements of the Ilium and Multivariate Adaptive Regression Splines (MARS) Models for Better Age Prediction. Forensic Sci. 2017; 62 (1): 18–29. DOI: 10.1111/1556-4029.13224.
47. Yusof NA, Soames RW, Cunningham CA, Black SM. Anat Rec (Hoboken). Growth of the human ilium: the anomalous sacroiliac junction 2013; 296 (11): 1688–94. DOI: 10.1002/ar.22785.
48. Schnitzler CM, Mesquita JM, Pettifor JM. Cortical bone development in black and white South African children: iliac crest histomorphometry. Bone. 2009; 44 (4): 603–11. DOI: 10.1016/j.bone.2008.12.009.
49. De Boer HH, Van der Merwe AE, Soerdjbalie-Maikoe VV. Human cranial vault thickness in a contemporary sample of 1097 autopsy cases: relation to body weight, stature, age, sex and ancestry. Int J Legal Med. 2016; 130 (5): 1371–7. DOI: 10.1007/s00414-016-1324-5.
50. Margulies S, Coats B. Experimental Injury Biomechanics of the Pediatric Head and Brain. In: Pediatric Injury Biomechanics. New York: Springer Science + Business Media, 2013; 157–190.
51. Li Z, Park BK, Liu W, Zhang J, Reed MP, Rupp JD, et al. A statistical skull geometry model for children 0–3 years old. PLoS One. 2015; 10 (5): e0127322. DOI: 10.1371/journal.pone.0127322. eCollection 2015.
52. Rodriguez-Florez N, Ibrahim A, Hutchinson JC, Borghi A, James G, Arthurs OJ, et al. Cranial bone structure in children with sagittal craniosynostosis: Relationship with surgical outcomes. J Plast Reconstr Aesthet Surg. 2017; 70 (11): 1589–97. DOI: 10.1016/j.bjps.2017.06.017.
53. Fazekas IGy. and Kósa F. Forensic Fetal Osteology. Budapest: Akadémiai Kiadó, 1978.
54. Sherer D, Sokolovski M, Dalloul M, Khoury-Collado F, Osho J, Lamarque M, et al. Fetal clavicle length throughout gestation: a nomogram. Ultrasound in Obstetrics and Gynecology. 2006; 27: 306–10.
55. McGraw MA, Mehlman CT, Lindsell CJ, Kirby CL. Postnatal growth of the clavicle: birth to eighteen years of age. Journal of Pediatric Orthopedics. 2009; 29: 937.
56. Black SM. and Scheuer JL. Age changes in the clavicle: from the early neonatal period to skeletal maturity. International Journal of Osteoarchaeology. 1996; 6: 425–34.
57. Bernat A, Huysmans T, Van Glabbeek F, Sijbers J, Gielen J, Van Tongel A. The anatomy of the clavicle: a three-dimensional cadaveric study. Clin Anat. 2014; 27 (5): 712–23.
58. Fujita T, Orimo H, Ohata M, Yoshikawa M. Changes in the cortical thickness of the clavicle according to age. J Am Geriatr Soc. 1968; 16 (4): 458–62.
59. Raziye D, Ceren U, Kadir D, Osman S, Mehmed Ali M. A Radiological Investigation on the Hand Development in Human Fetuses Throughout the Fetal Period and an Evaluation Performed in Terms of its Clinical Importance Hand Development. International Journal of Morphology. International Journal of Morphology. 2016; 34: 1539–52. DOI: 10.4067/s0717-95022016000400057.
60. Corrigan GE. The neonatal scapula. Biol Neonat. 1960; 2: 159–67. PubMed PMID: 13695677.
61. Hrdlicka A. The scapula: visual observations. Am J Phys Anthropol. 1942; 29: 73–94.
62. Vallois HV. L'omoplate humaine. Bulletin de la Sociétié d'Anthropolgie de Paris. 1946; 7: 16–99.

63. Saunders S, Hoppa R, Southern R. Diaphyseal growth in a nineteenth-century skeletal sample of subadults from St Thomas' Church, Belleville, Ontario. International Journal of Osteoarchaeology. 1993; 3: 265–81.
64. Xomutova E. Yu. Anatomiya shejnogo otdela pozvonochnika novorozhdennyx pri luchevyx metodax issledovaniya [dissertaciya]. Sankt-Peterburg, 2005. Russian.
65. Sharma N, Jain SK, Singh PK, Rohin Garg. A morphometric study of predictors for sexual dimorphism of cervical part of vertebral column in human fetuses. Journal of the Anatomical Society of India. 2017; 66: 135–39.
66. Kneissel M, Roschger P, Steiner W, Schamall D, Kalchhauser G, Boyde A, et al. Cancellous Bone Structure in the Growing and Aging Lumbar Spine in a Historic Nubian Population. Calcif Tissue Int. 1997; 61: 95–100.
67. Ponrartana S, Aggabao PC, Dharmavaram NL, Fisher CL, Friedlich P, Devaskar SU, et al. Sexual Dimorphism in Newborn Vertebrae and its Potential Implications. J Pediatr. 2015; 167: 416–21.
68. Borisov BK. Vesovye pokazateli razvitiya skeleta ploda cheloveka i soderzhanie v nem stronciya i kal'ciya. M.: Gosudarstvennyj komitet po ispol'zovaniyu atomnoj ehnergii SSSR, 1973; 14 s. Russian.

Литература

1. Degteva MO, Shagina NB, Vorobiova MI, Shishkina EA, Tolstykh EI, Akleyev AV. Contemporary Understanding of Radioactive Contamination of the Techa River in 1949–1956. Radiats Biol Radioecol. 2016; 56 (5): 523–34. English, Russian. PMID: 30703313.
2. Krestinina LY, Epifanova S, Silkin S, Mikryukova L, Degteva M, Shagina N, Akleyev A. Chronic low-dose exposure in the Techa River Cohort: risk of mortality from circulatory diseases. Radiat Environ Biophys. 2013; 52 (1): 47–57. DOI: 10.1007/s00411-012-0438-5. Epub 2012 Nov 4.
3. Аклеев А. В. Хронический лучевой синдром у жителей прибрежных сел реки Теча. Челябинск: Книга, 2012; 464 с.
4. Preston DL, Sokolnikov ME, Krestinina LY, Stram DO. Estimates of Radiation Effects on Cancer Risks in the Mayak Worker, Techa River and Atomic Bomb Survivor Studies. Radiat Prot Dosimetry. 2017; 173 (1–3): 26–31. DOI: 10.1093/rpd/ncw316.
5. O'Reilly SE, DeWeese LS, Maynard MR, Rajon DA, Wayson MB, Marshall EL, et al. An 13 image-based skeletal dosimetry model for the ICRP reference adult female-internal electron 14 sources. Phys Med Biol. 2016; 61 (24): 8794–8824. Epub 2016 Nov 29.
6. Xu XG, Chao TC, Bozkurt A. VIP-Man: an image-based whole-body adult male model constructed from color photographs of the Visible Human Project for multi-particle Monte Carlo calculations. Health Phys. 2000; 78 (5): 476–86. DOI: 10.1097/00004032-200005000-00003. PMID: 10772019.
7. Shah AP, Bolch WE, Rajon DA, Patton PW, Jokisch DW. A paired-image radiation transport model for skeletal dosimetry. J Nucl Med. 2005; 46 (2): 344–53. PMID: 15695796.
8. Pafundi D. Image-based skeletal tissues and electron dosimetry models for the ICRP reference pediatric age series. A dissertation presented to the graduate schools of the University of Florida in partial fulfillment of the requirements for the degree of doctor of the philosophy. University of Florida, 2009.
9. Hough M, Johnson P, Rajon D, Jokisch D, Lee C, Bolch W. An image-based skeletal dosimetry model for the ICRP reference adult male–internal electron sources. Phys Med Biol. 2011; 56 (8): 2309–46. DOI: 10.1088/0031-9155/56/8/001. Epub 2011 Mar 22.
10. Degteva MO, Tolstykh EI, Shishkina EA, Sharagin PA, Zalyapin VI, Volchkova AYu, et al. Stochastic Parametric Skeletal Dosimetry model for humans: General description. PlosOne; 2021 (submitted).
11. Sharagin PA, Shishkina EA, Tolstykh EI, Volchkova AYu, Smith MA, Degteva MO. Segmentation of hematopoietic sites of human skeleton for calculations of dose to active marrow exposed to bone-seeking radionuclides. In: RAD Conference Proceedings, 2018; (3): 154–8. DOI: 10.21175/RadProc.2018.33.
12. Шарагин П. А., Толстых Е. И., Шишкина Е. А., Дегтева М. О. Дозиметрическое моделирование кости для остеотропных бета-излучающих радионуклидов: размерные параметры и сегментация. В сборнике: Материалы международной научной конференции «Современные проблемы радиобиологии». Беларусь, Гомель, 23–24 сентября 2021. 2021; с. 200–204.
13. Толстых Е. И., Шарагин П. А., Шишкина Е. А., Дегтева М. О. Формирование доз облучения красного костного мозга человека от 89,90Sr, оценка параметров трабекулярной кости для дозиметрического моделирования. В сборнике: Материалы международной научной конференции «Современные проблемы радиобиологии». Беларусь, Гомель, 23–24 сентября 2021. 2021; с. 176–179.
14. Толстых Е. И., Шарагин П. А., Шишкина Е. А., Волчкова А. Ю. Дегтева М. О. Анатомо-морфологический базис для дозиметрического моделирования трабекулярной кости человека с использованием стохастического параметрического подхода. Клинический вестник ГНЦ ФМБЦ им. А. И. Бурназяна. 2022; 3: 25–40.
15. Shishkina EA, Timofeev YS, Volchkova AY, Sharagin PA, Zalyapin VI, Degteva MO, et al. Trabecula: A Random Generator of Computational Phantoms for Bone Marrow Dosimetry. Health Phys. 2020; 118 (1): 53–59. DOI: 10.1097/HP.0000000000001127.
16. Zalyapin VI, Timofeev YuS, Shishkina EA. A parametric stochastic model of bone geometry. Bulletin of Southern Urals State University, Issue «Mathematical Modelling. Programming & Computer Software» (SUSU MMCS). 2018; 11 (2): 44–57. DOI: 10.14529/mmp180204.
17. Cristy M. Active bone marrow distribution as a function of age in humans. Phys Med Biol. 1981; 26 (3): 389–400.
18. Vogler JB 3rd, Murphy WA. Bone marrow imaging. Radiology. 1988; 168 (3): 679–93.
19. Vande Berg BC, Malghem J, Lecouvet FE, Maldague B. Magnetic resonance imaging of the normal bone marrow. Skeletal Radiology. 1998; 27: 471–83.
20. Vande Berg BC, Malghem J, Lecouvet FE, Maldague B. Magnetic resonance imaging of normal bone marrow. Eur Radiol. 1998; 8 (8): 1327–34.
21. Taccone A, Oddone M, Dell'Acqua AD, Occhi M, Ciccone MA. MRI "road-map" of normal age-related bone marrow. II. Thorax, pelvis and extremities. Pediatr Radiol. 1995; 25 (8): 596–606; PubMed PMID: 8570312.
22. Taccone A, Oddone M, Occhi M, Dell'Acqua AD, Ciccone MA. MRI "road-map" of normal age-related bone marrow. I. Cranial bone and spine. Pediatr Radiol. 1995; 25 (8): 588–95; PubMed PMID: 8570311.
23. Cunningham C, Scheuer L, Black S. Developmental Juvenile Osteology. Elsevier Academic Press, 2016.
24. Robinson RA. Chemical analysis and electron microscopy of bone. In: Bone as a tissue, ed. by Rodahl K, Nicholson JT, Brown EM. New York: McGraw-Hill, 1960; p. 186–250.
25. Valentin J. Basic anatomical and physiological data for use in radiological protection: reference values. Annals of the ICRP. Annals of the ICRP. 32 (3–4): 1–277. 2002.
26. Медведев М. В. Ультразвуковая фетометрия: справочные таблицы и номограммы. М.: Реальное время, 2009; 19–24.
27. Florence JL. Linear and cortical bone dimensions as indicators of health status in subadults from the Milwaukee County Poor Farm Cemetery. M.A., University of Colorado at Denver, 2007.
28. Miles AEW. Growth Curves of Immature Bones from a Scottish Island Population of Sixteenth to mid-Nineteenth Century: Limb-bone Diaphyses and Some Bones of the Hand and Foot. International Journal of Osteoarcheology. 1994; 4: 121–36.
29. Maresh MM. Measurements from roentgenograms. In: Human Growth and Development (R.W. McCammon, Ed.). Springfield, IL: Charles C. Thomas, 1970; p. 157–200.
30. Jeanty P. Fetal limb biometry. Radiology. 1983; 147 (2): 601–2. DOI: 10.1148/radiology.147.2.6836145. PMID: 6836145.

31. Svadovsky VS. Age-related bone remodeling. Moscow, 1961.
32. Dhavale N, Halcrow SE, Buckley HR, Tayles N, Domett KM, Gray AR. Linear and appositional growth in infants and children from the prehistoric settlement of Ban Non Wat, Northeast Thailand: Evaluating biological responses to agricultural intensification in Southeast Asia, Journal of Archaeological Science: Reports. 2017; V11: 435–46.
33. Danforth ME, Wrobel GD, Armstrong CW, Swanson D. Juvenile age estimation using diaphyseal long bone lengths among ancient Maya populations. Latin American Antiquity. 2017; 20 (1): 3–13.
34. Beresheim AC, Pfeiffer S, Grynpas M. Ontogenetic changes to bone microstructure in an archaeologically derived sample of human ribs. J Anat. 2019. DOI: 10.1111/joa.13116.
35. Pfeiffer S. Cortical Bone Histology in Juveniles. Available from: https://www.researchgate.net/publication/303179375_Cortical_bone_histology_in_Juveniles
36. Hresko AM, Hinchcliff EM, Deckey DG, Hresko MT. Developmental sacral morphology: MR study from infancy to skeletal maturity. Eur Spine J. 2020. Available from: https://doi.org/10.1007/s00586-020-06350-6.
37. Mavrych V, Bolgova O, Ganguly P and Kashchenko S. Age-Related Changes of Lumbar Vertebral Body Morphometry. Austin J Anat. 2014; 1 (3): 7.
38. Dimeglio A, Bonnel F, Canavese F. The Growing Spine. In: Spinal Anatomy. Modern Concepts. Springer. 2020; 25–52.
39. Андронеску А. Анатомия ребенка. Бухарест: Меридиан, 1970.
40. Bernert Zs, Évinger S, Hajdu T. New data on the biological age estimation of children using bone measurements based on historical populations from the Carpathian Basin. Annales Historico-Naturales Musei Nationalis Hungarici. 2007; 99: 199–206.
41. Gindhart PS. Growth Standards for the Tibia and Radius in Children Aged One Month through Eighteen Years. Am J Phys Anthrop. 1973; 39: 41–48.
42. Suominen PK, Nurmi E, Lauerma K. Intraosseous access in neonates and infants: risk of severe complications - a case report. Acta Anaesthesiol Scand. 2015; 59 (10): 1389–93. DOI: 10.1111/aas.12602. Epub 2015 Aug 24. PubMed PMID: 26300243.
43. Blake KAS. An investigation of sex determination from the subadult pelvis: A morphometric analysis. Doctoral Dissertation, University of Pittsburgh. 2011.
44. Cunningham CA, Black SM. Iliac cortical thickness in the neonate — the gradient effect. J Anat. 2009; 215 (3): 364–70. DOI: 10.1111/j.1469-7580.2009.01112.x.
45. Cunningham CA, Black SM. Anticipating bipedalism: trabecular organization in the newborn ilium. J Anat. 2009; 214 (6): 817–29. DOI: 10.1111/j.1469-7580.2009.01073.x.
46. Corron L, Marchal F, Condemi S, Chaumoître K, Adalian P. A New Approach of Juvenile Age Estimation using Measurements of the Ilium and Multivariate Adaptive Regression Splines (MARS) Models for Better Age Prediction. Forensic Sci. 2017; 62 (1): 18–29. DOI: 10.1111/1556-4029.13224.
47. Yusof NA, Soames RW, Cunningham CA, Black SM. Anat Rec (Hoboken). Growth of the human ilium: the anomalous sacroiliac junction 2013; 296 (11): 1688–94. DOI: 10.1002/ar.22785.
48. Schnitzler CM, Mesquita JM, Pettifor JM. Cortical bone development in black and white South African children: iliac crest histomorphometry. Bone. 2009; 44 (4): 603–11. DOI: 10.1016/j.bone.2008.12.009.
49. De Boer HH, Van der Merwe AE, Soerdjbalie-Maikoe VV. Human cranial vault thickness in a contemporary sample of 1097 autopsy cases: relation to body weight, stature, age, sex and ancestry. Int J Legal Med. 2016; 130 (5): 1371–7. DOI: 10.1007/s00414-016-1324-5.
50. Margulies S, Coats B. Experimental Injury Biomechanics of the Pediatric Head and Brain. In: Pediatric Injury Biomechanics. New York: Springer Science + Business Media, 2013; 157–190.
51. Li Z, Park BK, Liu W, Zhang J, Reed MP, Rupp JD, et al. A statistical skull geometry model for children 0–3 years old. PLoS One. 2015; 10 (5): e0127322. DOI: 10.1371/journal.pone.0127322. eCollection 2015.
52. Rodriguez-Florez N, Ibrahim A, Hutchinson JC, Borghi A, James G, Arthurs OJ, et al. Cranial bone structure in children with sagittal craniosynostosis: Relationship with surgical outcomes. J Plast Reconstr Aesthet Surg. 2017; 70 (11): 1589–97. DOI: 10.1016/j.bjps.2017.06.017.
53. Fazekas IGy. and Kósa F. Forensic Fetal Osteology. Budapest: Akadémiai Kiadó, 1978.
54. Sherer D, Sokolovski M, Dalloul M, Khoury-Collado F, Osho J, Lamarque M, et al. Fetal clavicle length throughout gestation: a nomogram. Ultrasound in Obstetrics and Gynecology. 2006; 27: 306–10.
55. McGraw MA, Mehlman CT, Lindsell CJ, Kirby CL. Postnatal growth of the clavicle: birth to eighteen years of age. Journal of Pediatric Orthopedics. 2009; 29: 937.
56. Black SM. and Scheuer JL. Age changes in the clavicle: from the early neonatal period to skeletal maturity. International Journal of Osteoarchaeology. 1996; 6: 425–34.
57. Bernat A, Huysmans T, Van Glabbeek F, Sijbers J, Gielen J, Van Tongel A. The anatomy of the clavicle: a three-dimensional cadaveric study. Clin Anat. 2014; 27 (5): 712–23.
58. Fujita T, Orimo H, Ohata M, Yoshikawa M. Changes in the cortical thickness of the clavicle according to age. J Am Geriatr Soc. 1968; 16 (4): 458–62.
59. Raziye D, Ceren U, Kadir D, Osman S, Mehmed Ali M. A Radiological Investigation on the Hand Development in Human Fetuses Throughout the Fetal Period and an Evaluation Performed in Terms of its Clinical Importance Hand Development. International Journal of Morphology. International Journal of Morphology. 2016; 34: 1539–52. DOI: 10.4067/s0717-95022016000400057.
60. Corrigan GE. The neonatal scapula. Biol Neonat. 1960; 2: 159–67. PubMed PMID: 13695677.
61. Hrdlicka A. The scapula: visual observations. Am J Phys Anthropol. 1942; 29: 73–94.
62. Vallois HV. L'omoplate humaine. Bulletin de la Sociétié d'Anthropolgie de Paris. 1946; 7: 16–99.
63. Saunders S, Hoppa R, Southern R. Diaphyseal growth in a nineteenth-century skeletal sample of subadults from St Thomas' Church, Belleville, Ontario. International Journal of Osteoarchaeology. 1993; 3: 265–81.
64. Хомутова Е. Ю. Анатомия шейного отдела позвоночника новорожденных при лучевых методах исследования [диссертация]. Санкт-Петербург, 2005.
65. Sharma N, Jain SK, Singh PK, Rohin Garg. A morphometric study of predictors for sexual dimorphism of cervical part of vertebral column in human fetuses. Journal of the Anatomical Society of India. 2017; 66: 135–39.
66. Kneissel M, Roschger P, Steiner W, Schamall D, Kalchhauser G, Boyde A, et al. Cancellous Bone Structure in the Growing and Aging Lumbar Spine in a Historic Nubian Population. Calcif Tissue Int. 1997; 61: 95–100.
67. Ponrartana S, Aggabao PC, Dharmavaram NL, Fisher CL, Friedlich P, Devaskar SU, et al. Sexual Dimorphism in Newborn Vertebrae and its Potential Implications. J Pediatr. 2015; 167: 416–21.
68. Борисов Б. К. Весовые показатели развития скелета плода человека и содержание в нем стронция и кальция. М.: Государственный комитет по использованию атомной энергии СССР, 1973; 14 с.